Monthly Notices of the ROYAL ASTRONOMICAL SOCIETY

MNRAS **501,** 367–382 (2021) doi:10.1093/mnras/staa3677
Advance Access publication 2020 November 28

The bispectrum and 21-cm foregrounds during the Epoch of Reionization

Catherine A. Watkinson [1,2★] Cathryn M. Trott [3,4] and Ian Hothi[2]

[1]*School of Physics and Astronomy, Queen Mary University of London, Mile End Road, London E1 4NS, UK*
[2]*Department of Physics, Blackett Laboratory, Imperial College, London SW7 2AZ, UK*
[3]*International Centre for Radio Astronomy Research (ICRAR), Curtin University, 1 Turner Avenue, Bentley, WA 6102, Australia*
[4]*ARC Centre of Excellence for All Sky Astrophysics in 3 Dimensions (ASTRO 3D), Perth, WA 6845, Australia*

Accepted 2020 November 19. Received 2020 October 20; in original form 2020 February 14

ABSTRACT

Numerous studies have established the theoretical potential of the 21-cm bispectrum to boost our understanding of the Epoch of Reionization (EoR). We take a first look at the impact of foregrounds (FGs) and instrumental effects on the 21-cm bispectrum and our ability to measure it. Unlike the power spectrum for which (in the absence of instrumental effects) there is a window clear of smooth-spectrum FGs in which it may be detectable, there is no such 'EoR window' for the bispectrum. For the triangle configurations and scales we consider, the EoR structures are completely swamped by those of the FGs, and the EoR + FG bispectrum is entirely dominated by that of the FGs. By applying a rectangular window function on the sky combined with a Blackman–Nuttall filter along the frequency axis, we find that spectral, or in our case scale, leakage (caused by FFTing non-periodic data) suppresses the FG contribution so that cross-terms of the EoR and FGs dominate. While difficult to interpret, these findings motivate future studies to investigate whether filtering can be used to extract information about the EoR from the 21-cm bispectrum. We also find that there is potential for instrumental effects to seriously corrupt the bispectrum. FG removal using GMCA (generalized morphological component analysis) is found to recover the EoR bispectrum to a reasonable level of accuracy for many configurations. Further studies are necessary to understand the error and/or bias associated with FG removal before the 21-cm bispectrum can be practically applied in analysis of future data.

Key words: methods: statistical – intergalactic medium – dark ages, reionization, first stars – cosmology: theory.

1 INTRODUCTION

Understanding the properties of the first stars and galaxies, as well as their successors, is of high priority if we are to fully understand our Universe. Of particular interest is the Epoch of Reionization (EoR) during which these early generations of stars and galaxies progressively ionized the otherwise neutral intergalactic medium and (likely prior to the EoR) heated it during the Epoch of Heating (EoH). See Loeb & Furlanetto (2013) for a good review of these physical processes.

Many groundbreaking radio interferometers have been built (or are under development) that aim to map the 21-cm line of neutral hydrogen, either in emission or in absorption, as a function of redshift. Such data sets would ultimately provide 3D samples of our Universe and would revolutionize our understanding. The 21-cm hyperfine transition (produced by a spin flip in the lowest energy of neutral hydrogen) is sensitive to heating processes as we expect Lyman-alpha coupling to quickly couple the spin temperature to that of the kinetic gas temperature. Since the signal only comes from neutral hydrogen, it is also sensitive to the progress of reionization.

The first generation of interferometer such as LOFAR,[1] MWA,[2] and PAPER[3] are all hoping to make detections, but are currently limited by unresolved systematics to placing upper limits on the 21-cm power spectrum (Patil et al. 2017; Gehlot et al. 2019; Kolopanis et al. 2019; Mertens et al. 2020; Trott et al. 2020). There is hope that they will be able to get on top of systematics in order to integrate down the noise to make a detection of the EoR power spectrum. However, using just upper limits it has already been possible to place some constraints on the nature of reionization (Greig et al. 2020a, b). It is also worth noting that experiments to detect the global 21-cm signal have also been developed. Most notably, EDGES[4] has claimed a detection of an extreme trough in the signal during the EoH. If true, this requires us to look beyond our fiducial model for either exotic cooling mechanisms or a source of excess background with 21-cm wavelength (Bowman et al. 2018). It is consensus that another instrument needs to confirm the findings before we can be sure that EDGES has made a genuine detection (Hills et al. 2018; Bradley et al. 2019; Sims & Pober 2020).

It is expected that the next generation of radio interferometer, the SKA[5] and HERA,[6] will lead us into an era of precision high-redshift 21-cm observations (Braun et al. 2019). In preparation for these data sets, a great deal of effort continues to be poured into simulating the 21-cm signal so that we may robustly make sense of observations. The complexity of the physical processes involved means there is a

★ E-mail: catherine.watkinson@gmail.com
[1]The LOw Frequency ARray http://www.lofar.org/.
[2]The Murchison Wide-field Array http://www.mwatelescope.org/.
[3]The Precision Array to Probe Epoch of Reionization http://eor.berkeley.edu/.
[4]The Experiment to Detect the Global EoR Signature http://loco.lab.asu.edu/edges/.
[5]The Square Kilometre Array http://www.skatelescope.org/.
[6]The Hydrogen Epoch of Reionization Array http://reionization.org/.

great deal of degeneracy between different parameters involved in simulating the 21-cm signal (see e.g. Greig & Mesinger 2018; Park et al. 2018).

The 21-cm signal is predicted to be extremely non-Gaussian throughout the EoR. It therefore makes sense to consider the gains of using statistics like the bispectrum that are sensitive to non-Gaussian structure in data. The bispectrum is the Fourier dual to the three-point correlation function, which measures the excess probability of signal as a function of three points in a data set. This connection to three physical points in real space enforces the bispectrum to be a function of three $\boldsymbol{k}$ vectors that form a closed triangle. Many theoretical studies have shown that there is valuable additional information to be gained by measuring the bispectrum, e.g. Shimabukuro et al. (2016), Majumdar et al. (2017), Watkinson et al. (2019), Hutter et al. (2020), and Gorce & Pritchard (2019).

A major challenge to observing the 21-cm line is that there are strong radio foregrounds (FGs) at the frequencies of interest that are several orders of magnitude larger than the signal of interest. The work of Trott et al. (2019) also indicates that the bispectrum of certain $\boldsymbol{k}$-triangle configurations may be less FG corrupted than the power spectrum, and so exhibit higher signal to noise. This result was based on a theoretical model of the bispectrum Poisson-distributed point sources. However, synchrotron and free–free diffuse emissions from our Galaxy and extragalactic diffuse emission account for most of the 21-cm FGs at the redshifts of relevance to the EoR ($z \sim 6$–15) and beyond the cosmic dawn (Shaver et al. 1999; Di Matteo, Ciardi & Miniati 2004; Gleser, Nusser & Benson 2008; Liu & Tegmark 2012; Murray, Trott & Jordan 2017; Spinelli, Bernardi & Santos 2018).

In this work, we analyse the bispectrum from FGs that exhibit realistic structure on the sky, the cosmological signal, and the combination of both. We also consider how the bispectrum might be impacted by observations using the SKA by analysing the bispectrum of data that has been passed through the radio interferometer simulation OSKAR.[7] This work is a first step towards understanding how useable the bispectrum will be in practice for understanding the nature of the first stars and galaxies.

This paper is structured as follows. In Section 2, we provide an overview of the simulations we analyse in this paper and of the algorithm we use to measure the bispectrum. In Section 3, we consider whether or not there is an equivalent to the power spectrum EoR window for the bispectrum; we will see that while under some choices of window function the presence of EoR structures can alter the bispectrum from that of the FGs alone, there is not a clear-cut bispectrum EoR window. In Section 4, we take a look at the impact of simulating instrumental effects on the FG bispectrum, finding that there is potential for instrumentals to substantially corrupt the bispectrum from that of the underlying clean signal. Also in this section, we consider how much sample variance of the FGs might impact the FG bispectrum. We then consider how well FG removal using generalized morphological component analysis (GMCA) might be able to recover the clean EoR bispectrum in Section 5. We will see that GMCA EoR residuals exhibit a bispectrum with the correct sign and order of magnitude as that of the clean EoR signal, but not to the accuracy seen with the power spectrum. Finally, in Section 6 we detail our conclusions.

[7]Observational effects were simulated using OSKAR https://github.com/OxfordSKA/OSKAR.

2 OVERVIEW OF SIMULATIONS AND ANALYSIS

2.1 Foreground simulations

In this work, we utilize the FG simulations of Li et al. (2019b, hereafter Li2019) that extrapolate from lower redshift observations to produce FG simulations that exhibit realistic structures on the sky.[8] Li2019 include all the major contributions to the FGs mentioned in the previous section. Diffuse Galactic synchrotron is extrapolated to higher redshifts using the 408 MHz all-sky Haslam maps as a basis, with substructure simulated by extrapolation of the Galactic-emission power spectrum (Haslam 1983; Wang et al. 2010). Galactic free–free emission is assigned using its close relation to the Hα line as observed by Finkbeiner (2003) and extrapolating to higher redshifts. The Galactic diffuse emission was simulated at an (RA, Dec.) = (0°, −27°) which is at a high Galactic latitude appropriate for simulating an SKA observation (Beardsley et al. 2016). Semi-analytical modelling is employed for the less dominant FG contributors. Li2019 assume that point sources with a flux greater than 10 mJy (at 158 MHz) have been successfully removed. We refer the interested reader to Wang et al. (2010, 2013) and Li et al. (2019a) for details of the FG simulations.

2.2 Epoch of Reionization simulations

The Evolution of 21-cm Structure EoR data sets were used to generate the EoR skymaps, using the faint galaxies model.[9] These were tiled and resampled to match the FG simulation's resolution, namely 1800^2 pixels with a field of view $10° \times 10°$, giving a resolution of 20 arcsec. The Li2019 data sets consist of 101 frequency slices over the frequency range of 154–162 MHz. This frequency range corresponds to $z = 7.77$–8.22 and a channel width of 80 kHz; the central frequency is 158 MHz observing at $z = 8$ at which the neutral fraction of the EoR simulation is roughly 50 per cent.

2.3 Simulating observational effects

The FG and EoR skymaps were passed through the OSKAR simulation and then imaged using WS CLEAN[10] with natural weighting (Offringa et al. 2014) assuming the current design for the SKA-Low phase 1 telescope model, i.e. 224 stations (each of diameter 35 m containing 256 randomly placed antennas) randomly distributed in a core of diameter 1 km, with the remaining 288 stations occupying three spiral arms that extend out to a radius of 35 km (in clusters of 6).[11] They simulate a 6-h tracked observation to achieve a full uv-sampling without simulating noise to be more consistent with a 1000-h SKA integration time for which the noise level is expected to be negligible at $z \sim 8$. The final data sets analysed here are cropped from the simulated observation to have a $2° \times 2°$ field of view of 360^2 pixels. Li2019 also follow the above procedure for an (RA, Dec.) = (3°, −27°). We will refer to this simulated observation as 'observed'

[8]The simulations we analyse may be acquired from https://github.com/liweitianux/cdae-eor and the associated FG simulation package at https://github.com/liweitianux/fg21sim.

[9]The EoR simulations used were the faint galaxies model from http://homepage.sns.it/mesinger/EOS.html.

[10]Imaging was done using WS CLEAN https://sourceforge.net/p/wsclean.

[11]SKA1-Low layout used for the OSKAR telescope model was based on https://astronomers.skatelescope.org/wp-content/uploads/2016/09/SKA-TEL-SKO-0000422_02_SKA1_LowConfigurationCoordinates-1.pdf.

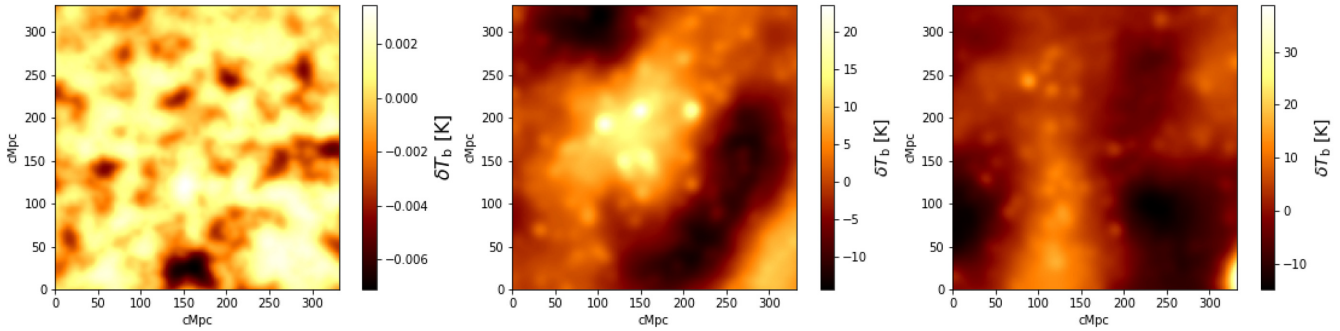

Figure 1. 154 MHz slice of the Li2019 data sets including simulated observations by SKA-LOW phase 1. The left plot shows the 'observed' EoR signal, the centre plot shows the 'observed' FGs in field 1, and the right plot shows the 'observed' FGs in field 2. These all correspond to a field of view of 2°.

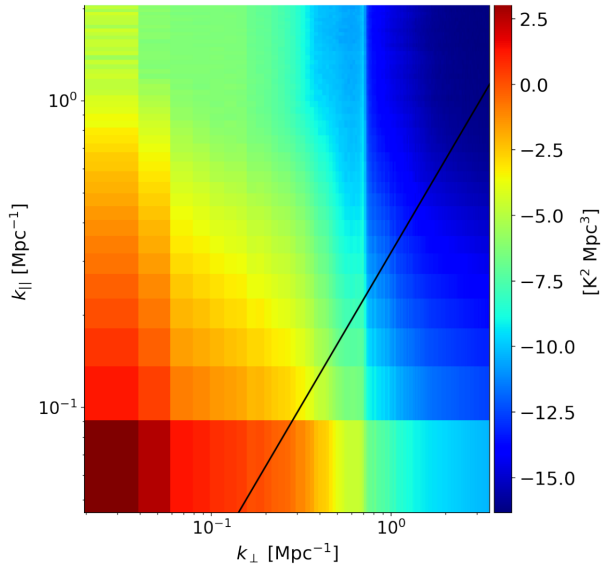

Figure 2. Logarithm of the power spectrum from the 'observed' EoR + FG (field 1) data set. For $k^{los} > 0.2$ cMpc^{-1}, the power spectrum is dominated by both the Galactic emission and EoR signal. We see an artefact at $k^{perp} \sim 0.7$ cMpc^{-1} and suppression of power for $k^{perp} > 0.7$ cMpc^{-1}. As such, we conservatively restrict our analysis to k vectors with $k < 0.6$ cMpc^{-1}. The black line marks the theoretical edge of the FG wedge; power in the wedge has been totally suppressed in this data set.

field 2 and the RA = 0° simulated observations as 'observed' field 1. Slices from the 'observed' field 1, field 2, and the EoR signal are shown in Fig. 1 for the 154 MHz slice.

We restrict the analysis that follows to $k < 0.6$ cMpc^{-1} because there is an artefact at this scale and a suppression of power beyond. This can be seen in Fig. 2, where we plot the power spectrum as a function of scale on the sky (k^{perp} or $k_\perp$) and in the line of sight (k^{los} or $k_{||}$). This artefact is produced at the imaging stage because Li2019 make a *uv* cut at 1000 λ, effectively erasing the power on smaller scales and therefore achieving a resolution similar to smaller arrays such as the MWA. This can be alleviated by using a Briggs weighting with a higher cutoff in baseline length. However, it is sufficient for studying EoR structures that are on larger scales.

2.4 Measuring the cylindrically averaged bispectrum

The bispectrum measures the level of correlation between three different scales defined by three k vectors $\boldsymbol{k}_1, \boldsymbol{k}_2, \boldsymbol{k}_3$ that form a closed triangle. The bispectrum is the Fourier dual to the real-space three-point correlation function (the excess probability as a function of three points) and is defined as,

$$(2\pi)^3 B(\boldsymbol{k}_1, \boldsymbol{k}_2, \boldsymbol{k}_3)\delta^{\mathrm{D}}(\boldsymbol{k}_1 + \boldsymbol{k}_2 + \boldsymbol{k}_3) = \langle \Delta(\boldsymbol{k}_1)\Delta(\boldsymbol{k}_2)\Delta(\boldsymbol{k}_3)\rangle\,, \quad (1)$$

where $\delta^{\mathrm{D}}(\boldsymbol{k}_1 + \boldsymbol{k}_2 + \boldsymbol{k}_3)$ is the Dirac-delta function.

The bispectrum provides some sensitivity to the presence of structure in a map, unlike the power spectrum that is unable to distinguish a data set with structure from a Gaussian random field. The interference pattern of the three plane waves associated with $\boldsymbol{k}_1, \boldsymbol{k}_2, \boldsymbol{k}_3$ for a given triangle configuration show the types of structure the bispectrum for that configuration is sensitive to. For example, the interference pattern of an equilateral triangle consists of regularly spaced filaments of above-average signal with circular cross-sections. The more the signal in a data set follows this interference pattern, the stronger the equilateral bispectrum will be relative to other configurations. Squashing the equilateral triangle configuration, so that one leg of the triangle is longer than the other two, squashes the circular cross-sections into elliptical cross-sections; at the extreme becoming almost planar. Squeezing the equilateral configuration so that one leg of the triangle is smaller modulates a large-scale mode over a smaller scale interference pattern. Should the structure in a map be driven by concentrations of below-average signal, rather than above-average signal, the bispectrum will be negative. We consider such interference patterns in more depth in Appendix C; see also Lewis (2011), Watkinson et al. (2019), and Hutter et al. (2020, in which fig. 1 is particularly useful) for more discussion of how to interpret of the bispectrum.

The bispectrum results in this paper are performed using an adapted version of the code described in Watkinson, Majumdar & Pritchard (2017) that exploits Fast-Fourier Transforms (FFTs) to enforce the Dirac-delta function to efficiently measure the spherically averaged bispectrum. The baselines of a radio interferometer sample *uv*-space (which is linearly related to $\boldsymbol{k}$ space). An observation by such an instrument will therefore produce a sampling of $\boldsymbol{k}^{perp}$, i.e. the $\boldsymbol{k}$ modes across the sky, for each frequency channel it observes. A Fourier Transform can then be performed in the frequency axis to produce a sampling of $\boldsymbol{k}^{los}$, i.e. the $\boldsymbol{k}$ modes along the line of sight. See Morales & Hewitt (2004) for the equations that connect the telescope observing coordinates to $\boldsymbol{k}$ in inverse comoving Mpc (cMpc^{-1}).

When measuring the bispectrum using equation (1), it is common to beat down statistical and instrumental noise by studying the spherically averaged bispectrum. In order for this to be a good approximation to that of performing an ensemble average, it is necessary that the data be homogeneous. This is not unreasonable

to assume for the cosmological signal if we ignore its frequency evolution, however for the FGs this is not the case. As such, performing spherical averaging will be a poor approximation and will average over information. Performing cylindrical averaging of modes around the line-of-sight axis, as is common in power spectrum studies, minimizes the impact of this. Also, the expectation that the FG power will be confined to large line-of-sight scales, makes it essential that we study the observed bispectrum as a cylindrically averaged quantity, i.e. averaging over angle around the line-of-sight axis.

The code of Watkinson et al. (2017) estimates $B(k_1, k_2, k_3)$ (the spherically averaged bispectrum) in the following manner:

(i) FFT the data set to $d^{\rm fft}$;

(ii) from this create three new masked data sets: $d_1^{\rm fft}$ containing the $d^{\rm fft}$ values in a spherical shell whose $|\boldsymbol{k}| \sim k_1$ and zero otherwise, $d_2^{\rm fft}$ containing the $d^{\rm fft}$ values in a spherical shell whose $|\boldsymbol{k}| \sim k_2$ and zero otherwise, and $d_3^{\rm fft}$ containing the $d^{\rm fft}$ values in a spherical shell whose $|\boldsymbol{k}| \sim k_3$ and zero otherwise;

(iii) create three other masked data sets $I_1^{\rm fft}$, $I_2^{\rm fft}$, $I_3^{\rm fft}$ as in the previous step, but with 1's instead of the $d^{\rm fft}$ values;

(iv) perform an inverse FFT on the $d_i^{\rm fft}$ and $I_i^{\rm fft}$ to produce d_i' and I_i';

(v) estimate $B(k_1, k_2, k_3)$ by summing over all pixels $(d_1' d_2' d_3')/(I_1' I_2' I_3')$ (applying a piecewise product) and applying Fourier normalizations.

The final two steps ensure that only triplets of pixels from $d_1^{\rm fft}$, $d_2^{\rm fft}$, and $d_3^{\rm fft}$ that form a closed triangle contribute to the final bispectrum. The reliability of this estimator therefore depends on the use of a sensible binning scheme for steps (ii) and (iii). There are many ways in which the binning of d_i and I_i might be adapted to instead measure the cylindrically averaged bispectrum.

After various tests we find that the optimal way is to use a binwidth of a fixed number of pixels when deciding whether a given pixel meets the requirement $|\boldsymbol{k}| \sim k_i$ for $i = 1, 2$; i.e. $|\boldsymbol{k}| = k_i \pm \Delta k$ where $\Delta k = nk_{\rm f}$, n is an integer, $k_{\rm f} = 2\pi/L_{\rm perp}$ is the fundamental pixel size in $\boldsymbol{k}$ space, and $L_{\rm perp}$ is the physical size of the simulation slices. Then in addition, we bin the closure vector's magnitude $|\boldsymbol{k}_3|$ using $\theta_{12} \pm 0.05\,\theta_{12}$ where θ_{12} is the triangle closure angle formed when adding $\boldsymbol{k}_1$ and $\boldsymbol{k}_2$.[12] Finally, we cut the spherical shells of the $d_i^{\rm fft}$ and $I_i^{\rm fft}$ into rings according to the $k^{\rm los}$ for each $\boldsymbol{k}_i \pm \Delta k'$, where $\Delta k' = mk_{\rm f}^{\rm los}$ to allow us to use a different integer m for different binning in the line of sight (important since the resolution in the line of sight is different to that on the sky, i.e. $k_{\rm f}^{\rm los} = 2\pi/L_{\rm los}$ where $L_{\rm los}$ is the physical size of the data along the frequency axis). In cutting spherical shells to produce rings at a particular line of sight, we ensure the k-vector triangles whose pixels contribute to the bispectrum are always of similar shape and size.

This operation essentially rotates a triangle configuration (such as that illustrated in Fig. 3) around the frequency or $k^{\rm los}$ axis. Other triangles exist in our k-space with the same shape, however to include them in the average would mix the line-of-sight information, which is exactly what we are seeking to avoid in taking a cylindrical average.[13] For each triangle with a positive $k^{\rm los}$, there is a twin configuration

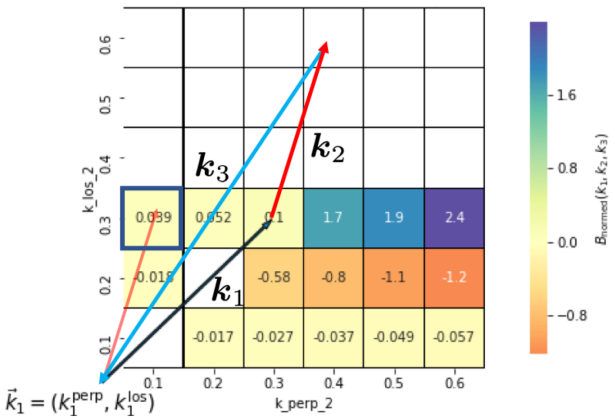

Figure 3. Schematic of how to interpret the triangle configurations for a particular square in $(k_2^{\rm perp}, k_2^{\rm los})$ space. The thick-lined black square indicates the bispectrum square that the illustrated $\boldsymbol{k}_1, \boldsymbol{k}_2, \boldsymbol{k}_3$ vector triangle corresponds to. In calculating the cylindrical average, we rotate a given triangle configuration around the $k^{\rm los}$ axis (and include the contribution for twin configurations with $-k_2^{\rm los}$ and $-k_1^{\rm los}$).

mirrored over the plane of the $k^{\rm perp}$ axis. As the sky is a real data set, we include the contributions of both of the positive and negative twin-triangle configurations as we rotate the triangle to calculate the average bispectrum for that configuration.

In tests using 21CMFAST simulations of the EoR signal (see Mesinger, Furlanetto & Cen 2011 for details of 21CMFAST) with different resolutions and initial conditions, we found that using ± 4 pixels, i.e. $\Delta k = 4k_{\rm f}$, provides optimal stability to sample variance. However, because the line-of-sight fundamental scale $k_{\rm f}^{\rm los}$ is relatively large due to the bandwidth of the Li2019 data set ($k_{\rm f}^{\rm los} = 0.05$ cMpc^{-1}), we bin $k^{\rm los}$ by $\pm 2k_{\rm f}^{\rm los}$ and $k^{\rm perp}$ by $\pm 4k_{\rm f}$, i.e. $\Delta k = 4k_{\rm f}$ and $\Delta k' = 2k_{\rm f}^{\rm los}$. This is reasonable in this case as we only consider one realization for the EoR. However, it would be better to ensure a finer line-of-sight k binning that allows for $\pm 4k_{\rm f}$ in any analysis that attempts to perform parameter estimation or similar. However, the evolution of the signal will become an issue for bandwidths much larger than 10 MHz.

We present our bispectrum results as a function of $k_2^{\rm perp}$ and $k_2^{\rm los}$ with each plot corresponding to a particular $\boldsymbol{k}_1 = (k_1^{\rm perp}, k_1^{\rm los})$. We annotate an arrow on to all plots to provide a visual description of $\boldsymbol{k}_1$ and each coloured square in our plots corresponds to a distinct triangle configuration. Fig. 3 illustrates how to interpret which $\boldsymbol{k}_1, \boldsymbol{k}_2, \boldsymbol{k}_3$ vector triangle configuration a given square (in the figure denoted by a black box) corresponds to. The vector for $\boldsymbol{k}_2$ is found by drawing an arrow from the origin of the $\boldsymbol{k}_1$ vector to the square of interest. This arrow is the $\boldsymbol{k}_2$ vector associated with the square. The triangle probed by this square can then be formed by transforming this arrow so that its origin follows from the end of the $\boldsymbol{k}_1$ arrow. For every plot of $\boldsymbol{k}_1 = (k_1^{\rm perp}, k_1^{\rm los})$ we show, we have examined three other plots corresponding to the set of triangles associated with $(k_1^{\rm perp}, -k_1^{\rm los})$, $(-k_1^{\rm perp}, k_1^{\rm los})$, and $(-k_1^{\rm perp}, -k_1^{\rm los})$.[14] This covers all configurations possible under the constraints of $(|k_1^{\rm perp}|, |k_1^{\rm los}|)$ and $(|k_2^{\rm perp}|, |k_2^{\rm los}|)$. As in Fig. 3, we

[12] Our choice for the binning of the closure vector $|\boldsymbol{k}_3|$ is motivated by previous tests in Watkinson et al. (2017, 2019).

[13] Our analysis also considered $\boldsymbol{k}_2$ vectors with $-k_2^{\rm perp}$. These configurations were included in the $(k_1^{\rm los}, -k_1^{\rm perp})$ configuration sets which are not explicitly included as the positive quadrant plots were sufficient to illustrate the main points we needed to make in this paper. We also considered the configuration sets associated with $(-k_1^{\rm los}, k_1^{\rm perp})$ and $(-k_1^{\rm los}, -k_1^{\rm perp})$ which covers all configurations for a given $(k_1^{\rm los}, k_1^{\rm perp})$.

[14] In our analysis, we work with $\boldsymbol{k}_1$ which is a 2D vector. $k_1^{\rm perp}$ is the projection of this vector on to the perpendicular axis (so can be described as a scalar) and similarly $k_1^{\rm los}$ is the projection of this vector on to the line-of-sight axis.

will only show the $\boldsymbol{k}_1 = (k_1^{\rm perp}, k_1^{\rm los})$ plots throughout this paper as they are sufficient to illustrate the key points that are raised in our analysis. We have also considered a range of $\boldsymbol{k}_1 = (k_1^{\rm perp}, k_1^{\rm los})$, but focus the presented analysis on ($k_1^{\rm perp} = 0.1$ cMpc^{-1}, $k_1^{\rm los} = 0.1$ cMpc^{-1}) and ($k_1^{\rm perp} = 0.3$ cMpc^{-1}, $k_1^{\rm los} = 0.3$ cMpc^{-1}) as again, these illustrate the main points we wish to convey in this paper as it is the FG $k_1^{\rm los}$ that dominates the effects we are mainly interested in here.[15]

Throughout this work, we present analysis using a normalized version of the bispectrum that is common in signal processing as it removes the amplitude part of the bispectrum to isolate the non-Gaussianity (Hinich & Clay 1968; Kim & Powers 1978; Hinich & Messer 1995; Hinich & Wolinsky 2005):

$$b(k_1, k_2, k_3) = \frac{B(k_1, k_2, k_3)}{\sqrt{(k_1\, k_2\, k_3)^{-1}\, P(k_1)\, P(k_2)\, P(k_3)}}\,. \tag{2}$$

Confirming Brillinger & Rosenblatt (1967) who argue that equation (2) is the optimal normalization choice for the bispectrum, Watkinson et al. (2019) find this to be the best normalization for interpreting the 21-cm bispectrum. We refer the interested reader to the appendix of Watkinson et al. (2019) for a detailed discussion of normalization choices for the bispectrum. It is worth noting that there are potential issues in using this statistic in practice if there are differences in the way that FG residuals (or instrumental effects) propagate on to the power spectrum and bispectrum estimators (Trott et al. 2019).

For the rest of this paper, when we refer to the bispectrum, we are referring to the normalized bispectrum of equation (2).

3 IS THERE AN EOR WINDOW FOR THE BISPECTRUM?

FGs at the frequencies relevant to 21-cm observations are all expected to get gradually stronger with decreasing observational frequency. With power coming from such large-scale frequency modes, it is expected that FG power will be restricted to small $k^{\rm los}$, with the chromatic nature of the instrument smearing some of the FG power into a wedge-like feature (Datta, Bowman & Carilli 2010; Morales et al. 2012; Vedantham, Udaya Shankar & Subrahmanyan 2012; Hazelton, Morales & Sullivan 2013; Thyagarajan et al. 2013; Liu, Parsons & Trott 2014). As such, there should be an EoR window largely clean of FGs in which the power spectrum from the EoR will dominate. Although, Li et al. (2019a) show that the presence of radio haloes could drastically reduce the signal to noise for $k < 1$ cMpc^{-1} even within the EoR window. In this section, we will consider whether or not such a window exists for the bispectrum; we analyse the bispectrum from the EoR signal (EoR-only), the FG signal (FG-only), and the combined field (EoR + FG). We emphasize that the normalized bispectrum (equation 2) of the EoR + FG signal cannot be considered as a simple sum of the EoR-only and FG-only bispectra. This is because the denominator and numerator change between the fields.

Before we consider instrumental effects on the bispectrum, we study the clean simulations so we may detangle which features are inherent and which relate to instrumental effects. Discrete Fourier Transforms, such as FFTW used in this study, all assume that the data they are analysing are infinite (for data of limited size, it effectively wraps the data around each axis so it is continuous; analogous to wrapping a sheet of paper into a cylinder). The data sets we analyse are non-periodic on all axis, i.e. a rectangular or top-hat window has been applied in real space. This means that there will be scale leakage (more commonly referred to as spectral leakage in the signal processing literature) when one performs a Fourier Transform on these data, especially as there is such a strong discontinuity as one wraps the frequency axis. In order to reduce such leakage and to optimize the information extracted by performing the Fourier Transform, it is common to apply some form of window function. Following works such as Li2019 and Chapman et al. (2016), we apply a Blackman–Nuttall filter to force periodicity along all axis. Although we note there are many other choices of window function that may be used, Gehlot et al. (2019) for example use the Hanning filter.

In Fig. 4, we present the cylindrically averaged bispectrum of the EoR-only (top), FG-only (middle), and EoR + FG (bottom) all from clean field 1, for ($k_1^{\rm perp}, k_1^{\rm los}$) = (0.1 cMpc^{-1}, 0.1 cMpc^{-1}). On larger scales ($k_2^{\rm los} = 0.1$), the FG bispectrum is strongly positive, as predicted by Trott et al. (2019) for smooth-spectrum point sources. However, the bispectrum is weakly negative $0.1 < k_2^{\rm los} < 0.3$, which implies that voids in the FG emission are driving the bispectrum on these scales. Despite the FG-only bispectrum being well confined to $k_2^{\rm los} \leq 0.2$ cMpc^{-1} and the EoR-only bispectrum being non-negligible and negative at $k_2^{\rm los} > 0.2$ cMpc^{-1}, the EoR structure has no discernible influence on the EoR + FG bispectrum for all triangle configurations for ($k_1^{\rm perp}, k_1^{\rm los}$) = (0.1 cMpc^{-1}, 0.1 cMpc^{-1}). This is because, although the level of non-Gaussianity in the EoR is high in the regions of triangle-configuration space where the FG non-Gaussianity is low, the absolute magnitude of the FG bispectrum is much greater (this can be seen explicitly in Fig. A1 in Appendix A).

In Fig. 5, we present the cylindrically averaged normalized bispectrum of EoR-only (top), and the filtered EoR + FG (middle) for ($k_1^{\rm perp}, k_1^{\rm los}$) = (0.3 cMpc^{-1}, 0.3 cMpc^{-1}). We see a very similar picture on these smaller scales, with emission driving a strong positive bispectrum for stretched configurations, and voids producing a low amplitude negative bispectrum as the triangle configurations become less stretched. We do not show the FG-only bispectrum here, as it is identical to the EoR + FG.

Having looked the bispectrum from the triangle configuration spaces associated with four other possible projections of $\boldsymbol{k}_1$ (namely ($k_1^{\rm perp}, -k_1^{\rm los}$), ($-k_1^{\rm perp}, k_1^{\rm los}$), and ($-k_1^{\rm perp}, -k_1^{\rm los}$)), we find that the FG bispectrum is strongest for the most squeezed and stretched triangle configurations both of which will pick up banded structures in data. For the interested reader, we further discuss the structures that drive the FG bispectrum in this data set in Appendix C.

3.1 Filtering to boost the contribution of the EoR to the bispectrum

In our first draft of this analysis, we followed Li2019 and Chapman et al. (2016) in applying the Blackman–Nuttall filter only to the frequency axis prior to measuring our statistics. Using a rectangular filter on the plane of the sky is not totally unreasonable for the cosmological signal because it exhibits a similar order of magnitude everywhere, i.e. the discontinuity is not strong. It is also not unreasonable for the FGs if you have used a Gaussian random field to simulate them (as is the case in Chapman et al. 2016). Regardless, scale leakage due to FFTing non-periodic data will be stronger when a rectangular window is used (Harris 1978). We find that filtering in this way highlights a potentially interesting result. We show the EoR + FG normalized bispectrum from the clean field with a Blackman–Nuttall filter applied only along the frequency axis in the bottom plot

[15] In our full analysis, we also considered ($k_1^{\rm perp} = 0.1$ cMpc^{-1}, $k_1^{\rm los} = 0.3$ cMpc^{-1}) and ($k_1^{\rm perp} = 0.3$ cMpc^{-1}, $k_1^{\rm los} = 0.1$ cMpc^{-1}).

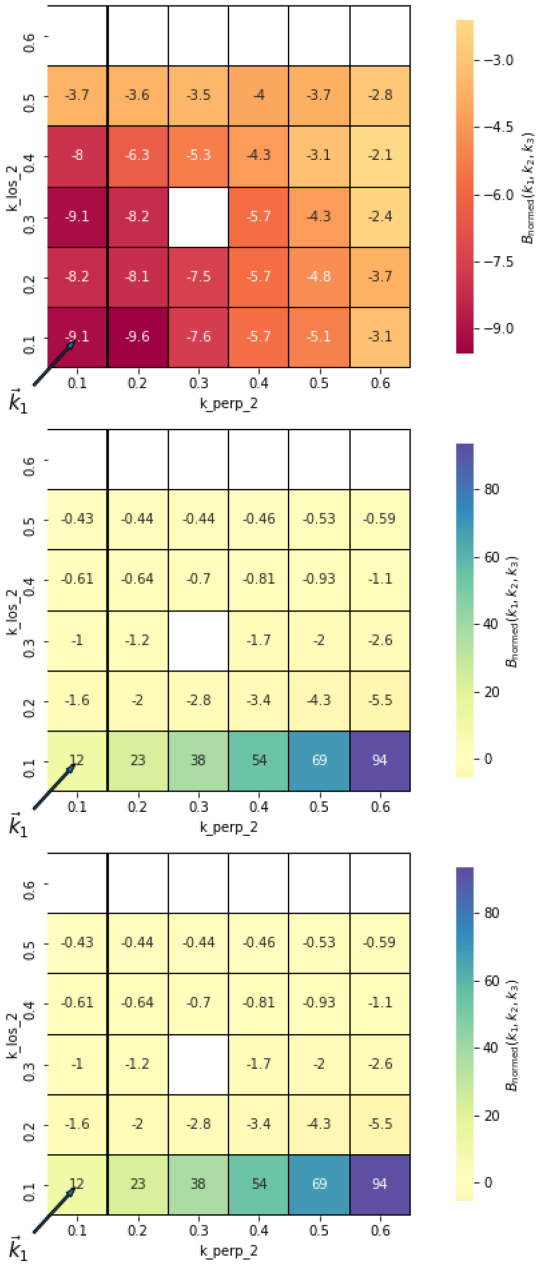

Figure 4. Normalized bispectrum from clean field 1 for $(k_1^{\mathrm{perp}}, k_1^{\mathrm{los}}) = (0.1\ \mathrm{cMpc}^{-1}, 0.1\ \mathrm{cMpc}^{-1})$ and for the EoR signal (*EoR-only; top*), the FGs signal (*FG-only; middle*), and for the combined field (*EoR + FG; bottom*). We plot this as a function of k_2^{perp} and k_2^{los} so that each square corresponds to a different $\boldsymbol{k}$-triangle configuration. There is no evidence of a clean window in which the EoR bispectrum dominates.

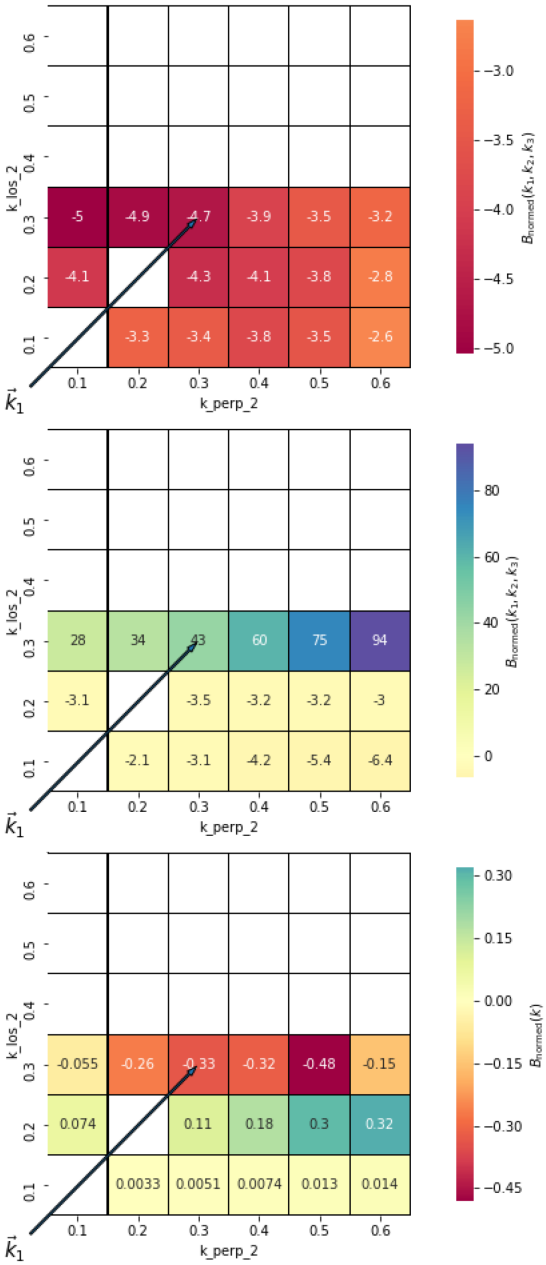

Figure 5. Normalized bispectrum from clean field 1 for $(k_1^{\mathrm{perp}}, k_1^{\mathrm{los}}) = (0.3\ \mathrm{cMpc}^{-1}, 0.3\ \mathrm{cMpc}^{-1})$ and for the EoR signal (*EoR-only; top*), for the combined field (*EoR + FG; middle*), and for the combined field but with Blackman–Nuttall filtering applied to the frequency axis only (*bottom*). We plot as a function of k_2^{perp} and k_2^{los} so that each square corresponds to a different $\boldsymbol{k}$-triangle configuration. While the presence of EoR structures does alter the bispectrum from that of the FG-only field when the data are only filtered along the frequency axis, it is difficult to interpret as there is no clean window in which the EoR bispectrum dominates.

of Fig. 5 for $(k_1^{\mathrm{perp}}, k_1^{\mathrm{los}}) = (0.3\ \mathrm{cMpc}^{-1}, 0.3\ \mathrm{cMpc}^{-1})$. This clearly has very different bispectrum characteristics to that seen from the fully filtered field, exhibiting a negative bispectrum for the most stretched configurations (i.e. those with $k_2^{\mathrm{perp}} = 0.3$) and with a much smaller amplitude. Clearly, the scale leakage is having a strong effect.

When we look at the cross-terms from the fields that have had the Blackman–Nuttall filter applied to the frequency axis only, we see that the FG bispectrum is strongly suppressed and the final signal is dominated by the FG–FG–FG, EoR–FG–FG, and EoR–EoR–FG cross bispectra (all of which contribute similar amplitudes, although they do differ in their sign). All other terms are negligible in their contribution (see Fig. A2 of Appendix A for plots of the contributing bispectrum components for this triangle configuration set).

While scale leakage is generally an undesirable effect, it is interesting that the influence of the EoR can be revealed using filtering and justifies further investigation as to whether this can be exploited somehow; either to extract the bispectrum of the cosmological

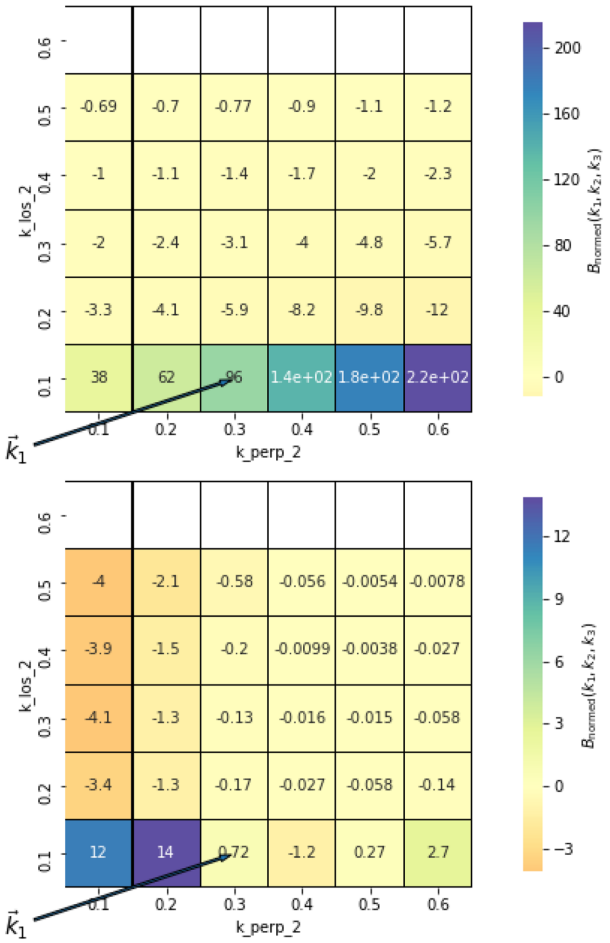

Figure 6. Normalized bispectrum for $(k_1^{\mathrm{perp}}, k_1^{\mathrm{los}}) = (0.3\ \mathrm{cMpc}^{-1},\ 0.1\ \mathrm{cMpc}^{-1})$ from clean FG-only (field 1; top) and from the 'observed' FG-only (field 1; bottom). We plot this as a function of k_2^{perp} and k_2^{los} so that each square corresponds to a different $\boldsymbol{k}$-triangle configuration. The simulation of observations suppresses the FG-only bispectrum, and qualitatively changes it from that of the clean field 1.

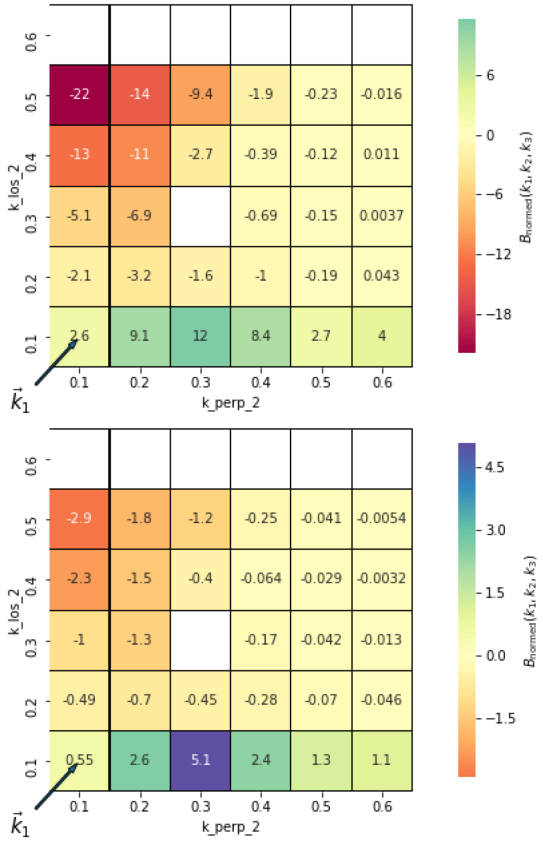

Figure 7. Normalized bispectrum for $(k_1^{\mathrm{perp}}, k_1^{\mathrm{los}}) = (0.1\ \mathrm{cMpc}^{-1},\ 0.1\ \mathrm{cMpc}^{-1})$ from 'observed' FG-only (field 1; top) and from 'observed' FG-only (field 2; bottom). This is the same field as the clean FG-only whose bispectrum is featured in the middle plot of Fig. 4. We plot this as a function of k_2^{perp} and k_2^{los} so that each square corresponds to a different $\boldsymbol{k}$-triangle configuration. Field 2 is qualitatively the same as field 1, but with a less extreme amplitude driven by lower contrast in signal (as seen in the maps of Fig. 1).

signal, or as a means to confirm a claimed detection with the power spectrum.

We conclude from the analysis in this section that the structure of the EoR gets washed out in the presence of strong FG non-Gaussianities, but that the influence of the EoR bispectrum can be seen if the data are filtered. So while there is no clear-cut EoR window for the bispectrum, there may still be a way to use the 21-cm bispectrum for detection verification (and perhaps even parameter estimation) if FG removal is not possible.

4 INSTRUMENTAL EFFECTS ON THE 21-CM BISPECTRUM

In this section, we consider to what degree the instrumentals might alter the bispectrum. Fig. 6 shows the bispectrum from the clean FG-only (field 1; top) and for the FG-only simulated observation (field 1; bottom) for the $(k_1^{\mathrm{perp}}, k_1^{\mathrm{los}}) = (0.3\ \mathrm{cMpc}^{-1},\ 0.1\ \mathrm{cMpc}^{-1})$ configuration set. We note that the bispectrum is far stronger for this set of configurations than it was for $(k_1^{\mathrm{perp}}, k_1^{\mathrm{los}}) = (0.1\ \mathrm{cMpc}^{-1},\ 0.1\ \mathrm{cMpc}^{-1})$ (see Fig. 4) and $(k_1^{\mathrm{perp}}, k_1^{\mathrm{los}}) = (0.3\ \mathrm{cMpc}^{-1},\ 0.3\ \mathrm{cMpc}^{-1})$ (see Fig. 5) and, as with $(k_1^{\mathrm{perp}}, k_1^{\mathrm{los}}) = (0.1\ \mathrm{cMpc}^{-1},\ 0.1\ \mathrm{cMpc}^{-1})$, is strongly positive for $k_1^{\mathrm{los}} < 0.2\ \mathrm{cMpc}^{-1}$ and weakly negative elsewhere in configuration space. The imprint of this OSKAR simulated instrumentals drastically suppresses the magnitude of the bispectrum, especially for $k_2^{\mathrm{perp}} > 0.2\ \mathrm{cMpc}^{-1}$, which alters it both quantitatively and qualitatively. After simulating observational effects, the bispectrum is strongest on larger scales ($k_2^{\mathrm{perp}} < 0.3\ \mathrm{cMpc}^{-1}$), whereas in the clean field it drops off monotonically from $k_2^{\mathrm{perp}} = 0.6\ \mathrm{cMpc}^{-1}$ until it is two ($k_2^{\mathrm{los}} = 0.2\ \mathrm{cMpc}^{-1}$) to three ($k_2^{\mathrm{los}} = 0.1\ \mathrm{cMpc}^{-1}$) orders of magnitude by $k_2^{\mathrm{perp}} = 0.1\ \mathrm{cMpc}^{-1}$. We also note the void induced negative bispectrum is boosted in amplitude for $k_2^{\mathrm{perp}} < 0.2$.

The boosting of the non-Gaussianity due to voids in the presence of instrumental effects is even stronger for cases where the positive bispectrum is less strong, i.e. where non-Gaussianity is less dominated by emission features, such as for the $(k_1^{\mathrm{perp}}, k_1^{\mathrm{los}}) = (0.1\ \mathrm{cMpc}^{-1}, 0.1\ \mathrm{cMpc}^{-1})$ configuration set. This can be seen by comparing the top plot of Fig. 7 in which we show the bispectrum from 'observed' field 1 to that of the clean field 1 (as seen in the middle plot of Fig. 4). The bispectrum in the region of $k_2^{\mathrm{perp}} < 0.3\ \mathrm{cMpc}^{-1}$, $k_2^{\mathrm{los}} > 0.3\ \mathrm{cMpc}^{-1}$ is between -10 and -20 in magnitude in 'observed' field 1, but is of the order of -1 in the clean field 1.

It is clear from this section that instrumental effects have the potential to alter the bispectrum drastically. However, in the absence of *uv* cutoff of 1000 λ (as performed in the imaging of the Li2019

data sets), the SKA imaging performance is exceptional, in both snapshot mode and with rotation synthesis. It is expected then that SKA images should be clean of sidelobes with little deconvolution required. As such the findings in this section are very much tentative, and motivate more detailed studies into the effects of instrumental effects on the bispectrum.

4.1 Foreground sample variance

As well as instrumental effects complicating our ability to interpret the 21-cm bispectrum, it is also prudent to consider the effects of sample variance on the bispectrum of the FGs. We therefore compare the bispectrum of 'observed' FG-only (field 2; shown in the bottom plot of Fig. 7) with that of the 'observed' FG-only field 1 (in the top plot of Fig. 7) for $(k_1^{\rm perp}, k_1^{\rm los}) = (0.1\ {\rm cMpc}^{-1}, 0.1\ {\rm cMpc}^{-1})$. We see that while the bispectra from these fields are qualitatively similar, the amplitude of the bispectrum is smaller in field 2. This is because the contrast between emission and voids of emission is less, as can be seen in the middle (field 1) and right (field 2) maps of Fig. 1. In field 2, apart from a very strong source of emission on the bottom right of the map (whose contribution will be strongly suppressed by the Blackman–Nuttall filter), the emission is mostly of the order of 10 K and in the voids of emission −10 K, whereas in field 1, the emission is of the order of 20 K over large regions of the map. It would be desirable to look at a slightly larger field of view, as 2° is a relatively conservative cropping choice for SKA. We again defer detailed consideration of this point to future work.

5 PROSPECTS FOR RECOVERING THE BISPECTRUM WITH FOREGROUND REMOVAL USING GMCA

Given that we have seen that there is no clear EoR window for the bispectrum as there is for the power spectrum, we take an initial look at the prospects at recovering the signal using FG removal. We apply GMCA to both the clean FG + EoR (field 1) to consider an ideal case, as well as the 'observed' FG + EoR (field 1). GMCA exploits sparseness of signals in a particular basis, here a wavelet deconstruction, in order to perform blind source separation (BSS). This BSS estimates a mixing matrix and signal combination that maximizes the sparseness of the signal. This produces a recovered signal and a noise residual. We refer the interested reader to Bobin et al. (2007, 2008, 2013) for details of this algorithm. Because the FGs are so many orders of magnitude greater than the EoR signal, GMCA works to recover the FG as the signal, leaving the EoR signal as part of the noise residuals. While GMCA technically performs BSS, it does require a little guidance in terms of being told how many statistically independent (linearly combined) components the signal, in our case the FGs, consists of. This is ultimately a free parameter; if too small the algorithm will struggle to accurately recover the signal, and if too large, it will overfit and might also recover the EoR signal; i.e. if it is not chosen correctly the algorithm will fail to separate the EoR signal out as residuals. For this work, we use four components that were found by Chapman et al. (2016) to be the optimal choice for recovering the power spectrum from OSKAR-simulated LOFAR data. We have experimented with a range of component numbers, and our initial findings agree with those of Chapman et al. (2016). However, we will perform a more thorough study of FG removal in the context of bispectrum recovery, including consideration of other FG removal methods than GMCA in a future study.

The top plot of Fig. 8 shows the $(k_1^{\rm perp}, k_1^{\rm los}) = (0.1\ {\rm cMpc}^{-1}, 0.1\ {\rm cMpc}^{-1})$ bispectrum of the residuals after running GMCA on clean

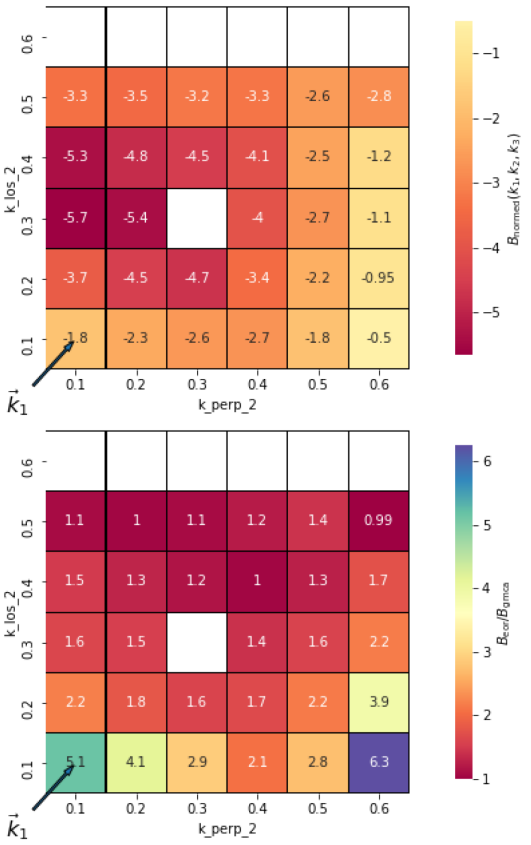

Figure 8. Normalized bispectrum from GMCA (four components) residuals from clean EoR + FG (field 1; top) for $(k_1^{\rm perp}, k_1^{\rm los}) = (0.1\ {\rm cMpc}^{-1}, 0.1\ {\rm cMpc}^{-1})$. We plot this as a function of $k_2^{\rm perp}$ and $k_2^{\rm los}$ so that each square corresponds to a different $\boldsymbol{k}$-triangle configuration. In the absence of instrumental effects, GMCA recovers the qualitative nature of the bispectrum in configuration space where $k_2^{\rm los} > 0.1$. The bottom plot shows the likeness ratio $B_{\rm eor}/B_{\rm gmca}$ of the GMCA-extracted bispectrum to the true bispectrum. We see there are certain configurations (mainly where $k_2^{\rm los} > 0.3$) for which the recovery is good with the likeness ratio being close to one.

EoR + FG (field 1) which, if working perfectly, would reproduce the clean EoR-only bispectrum. In the bottom plot of Fig. 8, we show the likeness ratio $B_{\rm eor}/B_{\rm gmca}$ of the bispectrum from clean EoR-only (field 1) to that of the GMCA residuals. Even in the absence of instrumental effects, GMCA does not qualitatively recover the bispectrum perfectly, with the bispectrum of the GMCA residuals being suppressed at $k_2^{\rm los} < 0.2$ relative to the clean EoR bispectrum. However, for the rest of configuration space it recovers the correct sign and order of magnitude that would still be useful information to have, so long as we can characterize the error and/or bias from FG removal. There are also certain configurations for which GMCA performs quite well at recovering the bispectrum for, for example, $k_2^{\rm los} = 0.5\ {\rm cMpc}^{-1}$ where we see the likeness ratios of the bottom plot of Fig. 8 are close to one.

We show the $(k_1^{\rm perp}, k_1^{\rm los}) = (0.3\ {\rm cMpc}^{-1}, 0.3\ {\rm cMpc}^{-1})$ bispectrum of the GMCA residuals and the likeness ratio in the top and bottom plots of Fig. 9, respectively. On such smaller scales, GMCA does a much better job of recovering the qualitative behaviour of the EoR bispectrum over configuration space, with its bispectrum consistently such that $B_{\rm eor}/B_{\rm gmca} \sim 1.0$ for all configurations.

We have seen that the bispectrum of the FGs is altered by the simulation of observational effects, it is therefore interesting to take

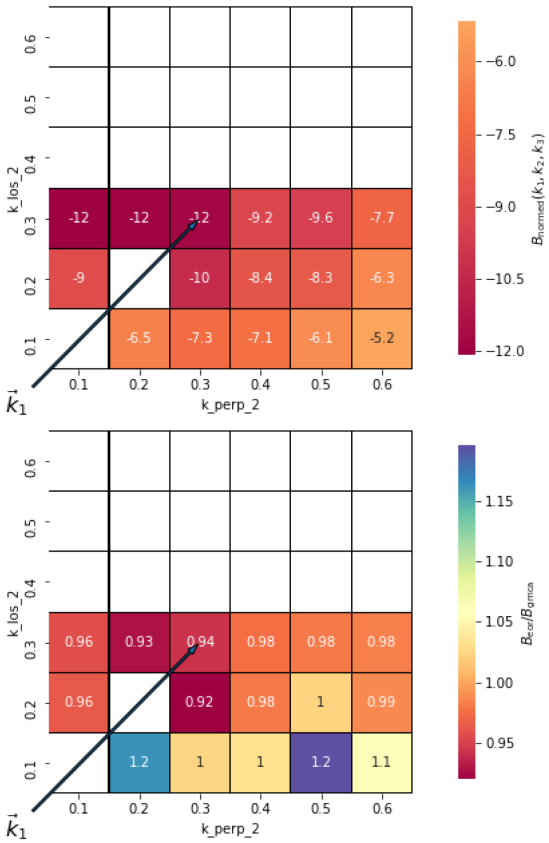

Figure 9. Normalized bispectrum from GMCA (four components) residuals from the clean EoR + FG (field 1; top) for $(k_1^{\mathrm{perp}}, k_1^{\mathrm{los}}) = (0.3\ \mathrm{cMpc}^{-1}, 0.3\ \mathrm{cMpc}^{-1})$. We plot this as a function of k_2^{perp} and k_2^{los} so that each square corresponds to a different $\boldsymbol{k}$-triangle configuration. The bottom plot shows the likeness ratio $B_{\mathrm{eor}}/B_{\mathrm{gmca}}$ of the GMCA-extracted bispectrum to the true bispectrum. For this configuration set, the qualitative recovery of the bispectrum is good.

a first look at how GMCA performs at recovering the bispectrum from the 'observed' Li2019 data sets. In the top plot of Fig. 10, we show the likeness ratio $B_{\mathrm{eor}}/B_{\mathrm{gmca}}$, here comparing the bispectrum from GMCA residuals from the 'observed' EoR + FG with the 'observed' EoR-only (both for field 1). While the bispectrum of the 'observed' EoR-only fields is not technically the quantity we are aiming to recover, the particular observation simulation we have analysed is potentially not typical, so it is useful to understand how well it can recover the 'observed' EoR-only bispectrum as well as that of clean EoR-only. It is also in principle possible to forward model the observation pipeline for parameter estimation purposes (although it remains to be seen how practical this is in reality). We see that GMCA recovers a bispectrum that is consistently about half that of the observed field for $k_2^{\mathrm{los}} < 0.3$, i.e. the likeness ratio is of the order of 2, beyond which the quality of the recovery drops (although there are a handful of configurations in this region for which the likeness ratio is close to 1).

In the middle plot of 10, we show $B_{\mathrm{eor}}/B_{\mathrm{gmca}}$ with B_{eor} being from clean EoR-only (field 1) and B_{gmca} from the residuals from the 'observed' field 1. Interestingly, the GMCA residuals from the 'observed' field 1 seem to exhibit a bispectrum that is closer to the true bispectrum for $k_2^{\mathrm{perp}} \leq 0.3\ \mathrm{cMpc}^{-1}$ and $k_2^{\mathrm{los}} \leq 0.4$ than the residuals from the clean field. It is possible then, that the instrumental corruption somehow aids the GMCA source separation on certain

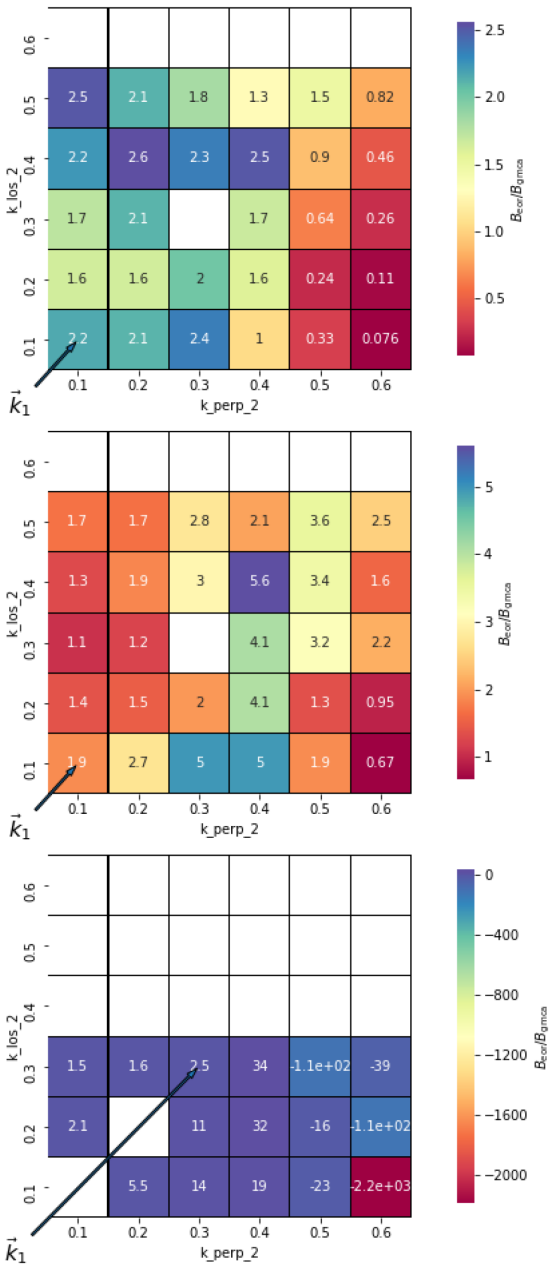

Figure 10. Likeness ratio $B_{\mathrm{eor}}/B_{\mathrm{gmca}}$ of the normalized bispectrum of 'observed' EoR-only (field 1) compared to that of the corresponding GMCA (four components) residuals from EoR + FG (top). The middle plot shows the likeness ratio of the clean EoR-only (field 1) bispectrum to that of the same GMCA residuals. Both top and middle are for the $(k_1^{\mathrm{perp}}, k_1^{\mathrm{los}}) = (0.1\ \mathrm{cMpc}^{-1}, 0.1\ \mathrm{cMpc}^{-1})$ configuration set. The bottom plot shows the likeness ratio between the clean EoR-only (field 1) and that of this field's GMCA residuals for the $(k_1^{\mathrm{perp}}, k_1^{\mathrm{los}}) = (0.3\ \mathrm{cMpc}^{-1}, 0.3\ \mathrm{cMpc}^{-1})$ configuration set. We plot this as a function of k_2^{perp} and k_2^{los} so that each square corresponds to a different $\boldsymbol{k}$-triangle configuration. GMCA seems to perform better at recovering the clean EoR-only bispectrum from the 'observed' field 1 for $k_2^{\mathrm{perp}} \leq 0.2\ \mathrm{cMpc}^{-1}$ and $k_2^{\mathrm{los}} \leq 0.4$, indicating that instrumental effects here modulate the FG field so that it is better described by four independent components. GMCA FG removal is less effective on smaller scales in the presence of instrumental effects as simulated here.

scales. This intuitively makes sense; for example, instrumental smoothing could simplify the FGs so that they are better described as four statistically independent components, i.e. the complexity of the FGs might be reduced by the inclusion of instrumental effects. It is of course also entirely possible, that this apparent improvement in performance is by chance. This point therefore warrants further investigation, which we will address in a future study.

The bottom plot of Fig. 10 shows the $(k_1^{\rm perp}, k_1^{\rm los}) = (0.3\ {\rm cMpc}^{-1}, 0.3\ {\rm cMpc}^{-1})$ likeness ratio for the GMCA residuals of 'observed' field 1 (again using the clean EoR signal for $B_{\rm eor}$). In contrast to what we saw with the clean field, GMCA does a worst job at recovering the bispectrum on these smaller scales, presumably this is due to the instrumental effects. The mode-mixing matrix GMCA uses to find the sparsest components is scale independent; as such, it is unable to describe these smaller scale effects. We find that likeness ratio using the observed EoR bispectrum for $(k_1^{\rm perp}, k_1^{\rm los}) = (0.3\ {\rm cMpc}^{-1}, 0.3\ {\rm cMpc}^{-1})$ for $B_{\rm eor}$ is similar to that of $(k_1^{\rm perp}, k_1^{\rm los}) = (0.1\ {\rm cMpc}^{-1}, 0.1\ {\rm cMpc}^{-1})$; i.e. of the order of 2 or less for $k_2^{\rm perp} \leq 0.4\ {\rm cMpc}^{-1}$, with the recovered bispectrum drastically suppressed relative to the observed EoR bispectrum beyond this. Again, we see that the clean signal is better recovered on the large scales, in this case for $k_2^{\rm perp} \leq 0.1\ {\rm cMpc}^{-1}$.

It would be remiss to judge our ability to recover the EoR bispectrum from the 'observed' data set discussed here without considering the associated GMCA recovery of the power spectrum. We do not include plots of the 2D power spectrum measured from GMCA residuals in the main text. We instead include them in Appendix B as they are interesting in their own right, but are not essential to our discussion. GMCA is excellent at recovering the clean EoR power spectrum for the scales we consider here. For all of the k-space we consider, the likeness ratio between the clean 2D power spectrum and that of the GMCA residuals is very close to 1. These results suggest that if we are to recover the EoR bispectrum to the same level of accuracy as the power spectrum, then we may need a better FG removal method than GMCA. The impact of bandwidth and number of channels on the quality of FG removal in the context of bispectrum recovery also needs to be considered in future works. Based on the findings of Carucci, Irfan & Bobin (2020), when applying GMCA to recover the power spectrum from intensity mapping data, it seems likely that increasing both will improve the quality of the bispectrum recovery. If improvements in our ability to recover the bispectrum are not possible, then an exhaustive study of the full range of triangle configurations could establish which are the least corrupted by FG residuals.

While it appears that GMCA cannot accurately recover the bispectrum from this data set for much of $k^{\rm perp}$–$k^{\rm los}$ space, there are other FG-removal algorithms such as the Gaussian processes method of Mertens, Ghosh & Koopmans (2018). There is also the promising option to use a convolutional denoizing auto-encoder to learn the features of the signal and therefore separate the signal from the FGs, as done by Li2019. It is quite possible that one of those or another FG-removal algorithm will do a better job than GMCA at recovering the EoR bispectrum. We will also consider this question further in a future study.

The FG simulations analysed here assume that point sources with a flux greater than 10 mJy have been removed. We have analysed the point-source 21-cm bispectrum as predicted by Trott et al. (2019), and find that the bispectrum will be boosted in magnitude (relative to that of the Li2019 FGs) if point source is not so effectively removed. For example, if we assume that only point sources with a flux greater than 50 mJy can be removed, then the maximum normalized bispectrum can be as high as 10^4 for $(k_1^{\rm perp}, k_1^{\rm los}) = (0.1\ {\rm cMpc}^{-1}, 0.1\ {\rm cMpc}^{-1})$ and 10^{56} for $(k_1^{\rm perp}, k_1^{\rm los}) = (0.3\ {\rm cMpc}^{-1}, 0.3\ {\rm cMpc}^{-1})$. It is therefore important that alongside developing an understanding of the impact of FG residuals on the 21-cm bispectrum, that we also understand the impact of point-source removal residuals.

6 CONCLUSION

In this paper, we have measured the bispectrum from accurate simulations of 21-cm FGs, a typical Epoch of Reionisation simulation, and their combination. We have also measured the bispectrum from these data sets after having been passed through an SKA telescope observation pipeline (consisting of OSKAR + WS CLEAN).

Through our analysis, we have established that there is not a clean EoR window for the bispectrum (at least for the configurations we have considered here), this means that (unlike with the power spectrum) FG avoidance is not obviously a viable approach to constrain the 21-cm EoR bispectrum. By exploiting the scale leakage caused by using a rectangular filter on plane of the sky combined with a Blackman–Nuttall filter along the frequency axis, EoR structure can alter the bispectrum of the combined field from that of the FG-only field on smaller scales. Interpreting this contribution is highly challenging, however our findings motivate investigations into other filtering schemes to see if the EoR bispectrum might be extracted in such a manner as to be useful either for parameter estimation or as a detection confirmation.

We find that including OSKAR-simulated instrumental effects suppresses the bispectrum on small scales (although we note the resolution considered here is lower than that SKA is capable of achieving) and boosts the negative bispectrum driven by large voids of emission. The findings of this paper motivate further study to understand the subtleties of instrumental effects on the 21-cm bispectrum. Even if it transpires, these studies find the bispectrum cannot be used to constrain the underlying EoR signal, it may well be that the bispectrum will instead be useful for refining our processing of observed data more precisely.

Given the absence of an EoR window for the bispectrum, we take an initial look at whether FG removal using GMCA can accurately recover the non-Gaussianities of the EoR signal. We assume four independent components to describe and fit the FG signal, which under perfect performance should return the EoR signal in its noise residuals. The bispectrum of the GMCA residuals from the clean simulations is qualitatively similar to that of the clean EoR signal. Their amplitude is also of the correct order of magnitude. The quality of the recovery does however drop on larger scales ($k_2^{\rm los} < 0.2\ {\rm cMpc}^{-1}$) for $\boldsymbol{k}_1 = (0.1\ {\rm cMpc}^{-1}, 0.1\ {\rm cMpc}^{-1})$. When GMCA is applied to the simulated observations, on larger scales ($k^{\rm perp} \leq 0.2\ {\rm cMpc}^{-1}$ and $k^{\rm los} \leq 0.4\ {\rm cMpc}^{-1}$), the bispectrum of its residuals are closer to those of the clean EoR signal than the GMCA residuals from the clean EoR + FG field. This is likely because, on these scales, the instrumental effects simplify the FG signal so that it is more cleanly described as four linearly independent components, as assumed by GMCA. However, on smaller scales ($k^{\rm perp} > 0.3\ {\rm cMpc}^{-1}$), GMCA fails entirely to recover the bispectrum of the EoR. It is worth noting that for this data set, GMCA does a substantially better job at recovering the 2D power spectrum. Nevertheless, these findings are encouraging and motivate more detailed studies to establish how effective GMCA and other FG removal algorithms are at the level of the bispectrum.

There is an important caveat to this study that is worth bearing in mind and should be addressed in future studies. For the simulated observations analysed here, there is a corruption to the signal that

presents as a thin band of excess power at $k^{\rm perp} \sim 0.7$ cMpc^{-1} and a suppression of power beyond. This is caused by a λ cut at the imaging stage. Although we have omitted all modes where $k^{\rm perp} > 0.6$ to avoid this corruption, it remains unclear how much this is causing the corruption of the bispectrum by instrumentals discussed in this paper. Furthermore, while our analysis covers a wide range of configurations and scales, within the restrictions of working in the $k^{\rm perp}$–$k^{\rm los}$ space, it is not exhaustive. In particular, it has not been possible to investigate the smaller scales available to the SKA with the data sets analysed. Future studies should address this.

Despite these caveats, the conclusions in this paper are on solid ground and motivate further work to understand exactly how we might use the bispectrum in practice. The rewards of such studies are a potentially more robust and accurate understanding of the first stars and galaxies, and/or an important tool for improving our processing of 21-cm observations.

ACKNOWLEDGEMENTS

The authors would like to thank the anonymous referee for their useful comments; through these, you have improved the paper a great deal. CAW's research is currently supported by a UK Research and Innovation Future Leaders Fellowship, grant number MR/S016066/1. However, the research presented in this paper was carried out with financial support from the European Research Council under ERC grant number 638743-FIRSTDAWN (held by Jonathan Pritchard). CAW also thanks Weitan Li for making his data sets and analysis pipelines publicly available and for providing such good documentation. CAW also thanks the ARC Centre for Excellence in All-Sky Astrophysics in 3D Visitor Fund for facilitating this collaboration. CMT acknowledges financial support from an ARC Future Fellowship under grant FT180100321. IH acknowledges studentship funding from the Royal Society Dorothy Hodgkin Fellowship (held by Emma Chapman). IH also thanks Emma Chapman for her ongoing mentorship. This research was partly supported by the Australian Research Council Centre of Excellence for All Sky Astrophysics in 3 Dimensions (ASTRO 3D), through project number CE170100013.

DATA AVAILABILITY

The data we analyse in this paper may be acquired from https://github.com/liweitianux/cdae-eor and the associated FG simulation package at https://github.com/liweitianux/fg21sim. The bispectrum code used to make the analysis maybe found at https://bitbucket.org/caw11/bifft/src/master/.

REFERENCES

Beardsley A. P. et al., 2016, ApJ, 833, 21
Bobin J., Starck J. L., Fadili J., Moudden Y., 2007, IEEE Trans. Image Process., 16, 2662
Bobin J., Moudden Y., Starck J. L., Fadili J., Aghanim N., 2008, Stat. Methodol., 5, 307
Bobin J., Starck J. L., Sureau F., Basak S., 2013, A&A, 550, A73
Bowman J. D., Rogers A. E. E., Monsalve R. A., Mozdzen T. J., Mahesh N., 2018, Nature, 555, 67
Bradley R. F., Tauscher K., Rapetti D., Burns J. O., 2019, ApJ, 874, 153
Braun R., Bonaldi A., Bourke T., Keane E., Wagg J., 2019, preprint (arXiv: 1912.12699)
Brillinger D., Rosenblatt M., 1967, in Bernard H., ed., Spectrum Analysis of Time Series. Wiley, New York, p. 189
Carucci I. P., Irfan M. O., Bobin J., 2020, MNRAS, 499, 304
Chapman E., Zaroubi S., Abdalla F. B., Dulwich F., Jelić V., Mort B., 2016, MNRAS, 458, 2928
Datta A., Bowman J. D., Carilli C. L., 2010, ApJ, 724, 526
Di Matteo T., Ciardi B., Miniati F., 2004, MNRAS, 355, 1053
Finkbeiner D. P., 2003, ApJS, 146, 407
Gehlot B. K. et al., 2019, MNRAS, 488, 4271
Gleser L., Nusser A., Benson A. J., 2008, MNRAS, 391, 383
Gorce A., Pritchard J. R., 2019, MNRAS, 489, 1321
Greig B., Mesinger A., 2018, IAUS, 333, 18
Greig B. et al., 2020a, MNRAS, Available at: https://doi.org/10.1093/mnras/staa3593
Greig B., Trott C. M., Barry N., Mutch S. J., Pindor B., Webster R. L., Wyithe J. S. B., 2020b, MNRAS, Available at: https://doi.org/10.1093/mnras/staa3494
Harris F., 1978, Proc. IEEE, 66, 51
Haslam C. G. T., 1983, Observatory, 103, 133
Hazelton B. J., Morales M. F., Sullivan I. S., 2013, ApJ, 770, 156
Hills R., Kulkarni G., Meerburg P. D., Puchwein E., 2018, Nature, 564, 32
Hinich M. J., Clay C. S., 1968, Rev. Geophys., 6, 347
Hinich M., Messer H., 1995, IEEE Trans. Signal Process., 43, 2130
Hinich M. J., Wolinsky M., 2005, J. Stat. Plan. Inference, 130, 405
Hutter A., Watkinson C. A., Seiler J., Dayal P., Sinha M., Croton D. J., 2020, MNRAS, 492, 653
Kim Y. C., Powers E. J., 1978, Phys. Fluids, 21, 1452
Kolopanis M. et al., 2019, ApJ, 883, 133
Lewis A., 2011, J. Cosmol. Astropart. Phys., 10, 1475
Li W. et al., 2019a, ApJ, 879, 104
Li W. et al., 2019b, MNRAS, 485, 2628 (Li2019)
Liu A., Tegmark M., 2012, MNRAS, 419, 3491
Liu A., Parsons A. R., Trott C. M., 2014, Phys. Rev. D, 90, 023018
Loeb A., Furlanetto S. R., 2013, The First Galaxies in the Universe. Princeton Univ. Press, Princeton, p. 540
Majumdar S., Pritchard J. R., Mondal R., Watkinson C. A., Bharadwaj S., Mellema G., 2017, MNRAS, 476, 4007
Mertens F. G., Ghosh A., Koopmans L. V. E., 2018, MNRAS, 478, 3640
Mertens F. G. et al., 2020, MNRAS, 493, 1662
Mesinger A., Furlanetto S. R., Cen R., 2011, MNRAS, 411, 955
Morales M. F., Hewitt J., 2004, ApJ, 615, 7
Morales M. F., Hazelton B., Sullivan I., Beardsley A., 2012, ApJ, 752, 137
Murray S. G., Trott C. M., Jordan C. H., 2017, ApJ, 845, 7
Offringa A. R. et al., 2014, MNRAS, 444, 606
Park J., Mesinger A., Greig B., Gillet N., 2018, MNRAS, 484, 933
Patil A. H. et al., 2017, ApJ, 838, 65
Shaver P. A., Windhorst R. A., Madau P., de Bruyn A. G., 1999, A&A, 345, 380
Shimabukuro H., Yoshiura S., Takahashi K., Yokoyama S., Ichiki K., 2016, MNRAS, 468, 1542
Sims P. H., Pober J. C., 2020, MNRAS, 492, 22
Spinelli M., Bernardi G., Santos M. G., 2018, MNRAS, 479, 275
Thyagarajan N. et al., 2013, ApJ, 776, 6
Trott C. M. et al., 2019, Publ. Astron. Soc. Aust., 36, e023
Trott C. M. et al., 2020, MNRAS, 493, 4711
Vedantham H., Udaya Shankar N., Subrahmanyan R., 2012, ApJ, 745, 176
Wang J. et al., 2010, ApJ, 723, 620
Wang J. et al., 2013, ApJ, 763, 90
Watkinson C. A., Majumdar S., Pritchard J. R., 2017, MNRAS, 472, 2436
Watkinson C. A. et al., 2019, MNRAS, 482, 2653

APPENDIX A: THE UNNORMALIZED AND CROSS-BISPECTRUM

In Fig. A1, we show the unnormalized bispectrum for the EoR-only (left), FG-only (middle), and EoR + FG (right) (a Blackman–Nuttall filter has been applied to all axis for these). We include the bispectra for $(k_1^{\rm perp}, k_1^{\rm los}) = (0.1\ {\rm cMpc}^{-1}, 0.1\ {\rm cMpc}^{-1})$ in the top row and $(k_1^{\rm perp}, k_1^{\rm los}) = (0.3\ {\rm cMpc}^{-1}, 0.3\ {\rm cMpc}^{-1})$ in the bottom row. It is clear, for these configuration sets, that the FG component completely

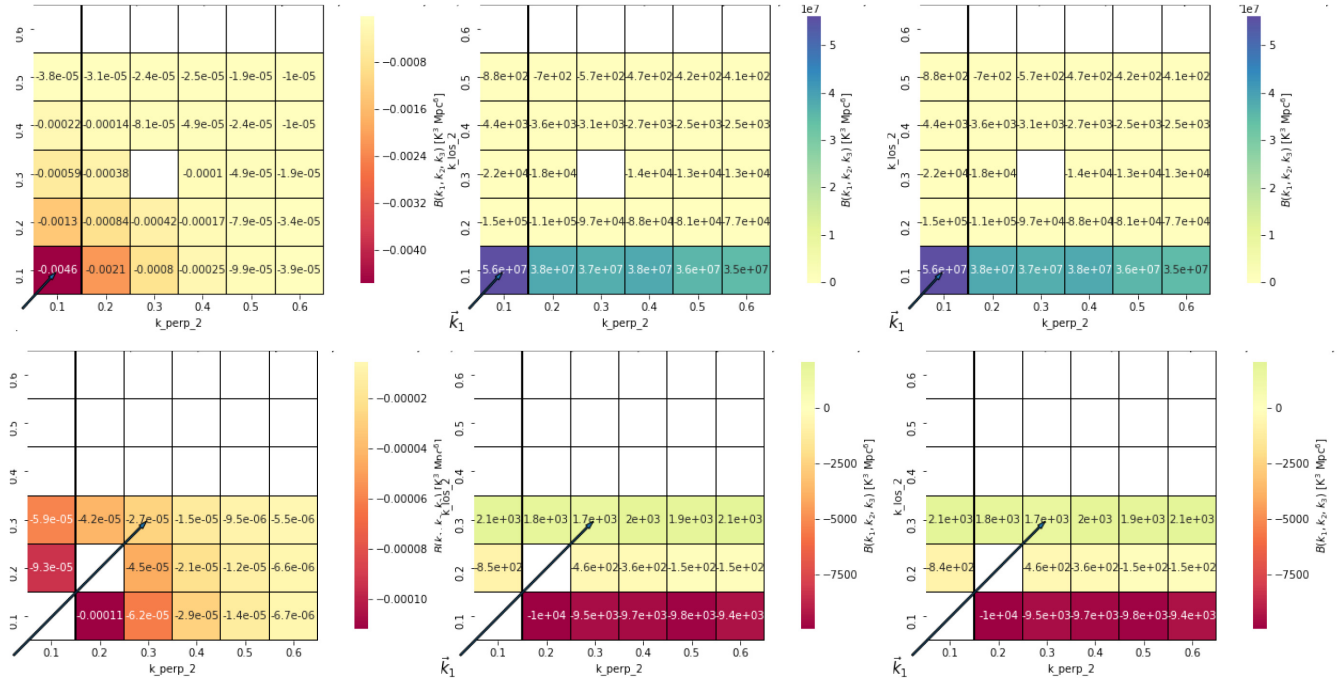

Figure A1. Unnormalized bispectrum for $(k_1^{\rm perp}, k_1^{\rm los}) = (0.1\ {\rm cMpc}^{-1}, 0.1\ {\rm cMpc}^{-1})$ in the top row and $(k_1^{\rm perp}, k_1^{\rm los}) = (0.3\ {\rm cMpc}^{-1}, 0.3\ {\rm cMpc}^{-1})$ in the bottom row. The left column contains the EoR-only bispectra, the middle the FG-only bispectra, and the right column the EoR + FG bispectra. We see that the FGs totally dominate the bispectrum in terms of magnitude.

dominates in terms of magnitude and drives the bispectrum of the EoR + FG field, shown in the middle plot of Fig. 5 in the main text. Note this is equally clear in plots of the normalized bispectrum for which the power spectrum of the combined field has been used in the normalization (as is appropriate when considering the contribution of the EoR to the EoR + FG bispectrum).

For any $X(x) = F(x) + S(x)$, where the FGs $F(x)$ and cosmological signal $S(x)$ can be filtered or unfiltered fields, the bispectrum can be written as

$$\begin{aligned} B^{XXX} &= \langle X(\boldsymbol{k}_1)X(\boldsymbol{k}_2)X(\boldsymbol{k}_3)\rangle \\ &= B^{FFF} + B^{FFS} + B^{FSF} + B^{FSS} + B^{SFF} + B^{SFS} \\ &\quad +, B^{SSF} + B^{SSS}. \end{aligned} \tag{A1}$$

If we are to normalize according to equation (2), then the normalization for all of the components should be the same, and use the power spectrum of the combined field X.

In Fig. A2, we show the cross-bispectrum components that contribute to the EoR + FG field that has been filtered along the frequency axis only. Using a rectangular window on the sky produces scale leakage that boosts the influence of the EoR, with the normalized bispectrum of EoR + FG (shown in the bottom plot of Fig. 5) being dominated by the FG–FG–FG, EoR–EoR–FG, and EoR–FG–FG components, with each contributing similar amplitudes.

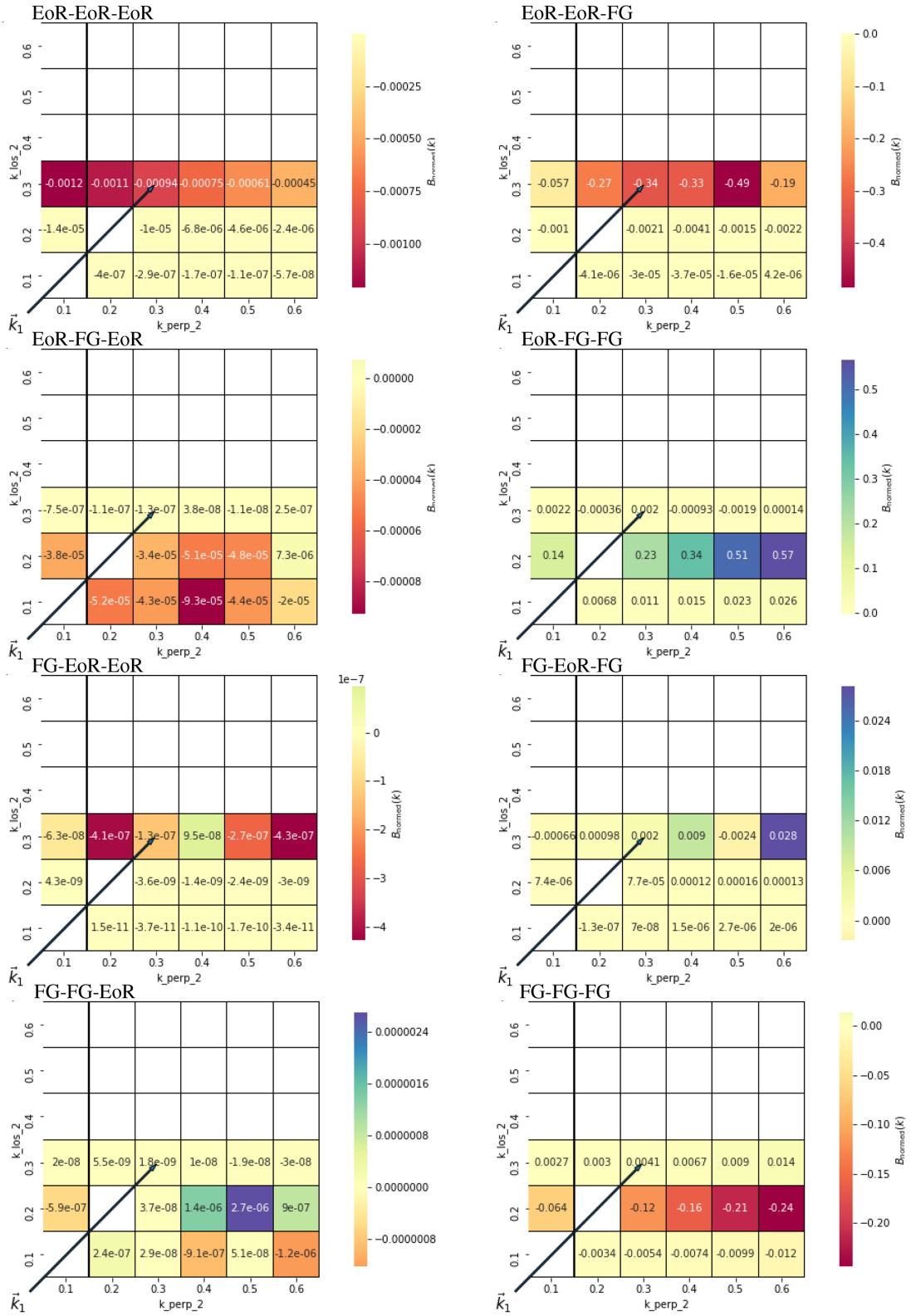

Figure A2. We plot the cross-bispectrum of the EoR and FG fields filtered by the Blackman–Nuttall filter in the frequency direction only. The bispectrum of the combined field is the linear sum of these. We see that once filtered, the EoR–FG–FG and EoR–EoR–FG dominate the bispectrum of the EoR + FG bispectrum.

APPENDIX B: GMCA RECOVERY OF POWER SPECTRUM

In this appendix, we look at how well GMCA residuals represent the EoR 2D power spectrum. The 2D power spectrum of GMCA residuals provides a very good representation of that of the clean EoR signal, as can be seen in Fig. B1. This plot shows the 2D power spectrum for the clean EoR signal (left), the GMCA residuals assuming four components to describe the FG signal (middle), and their likeness ratio (right).

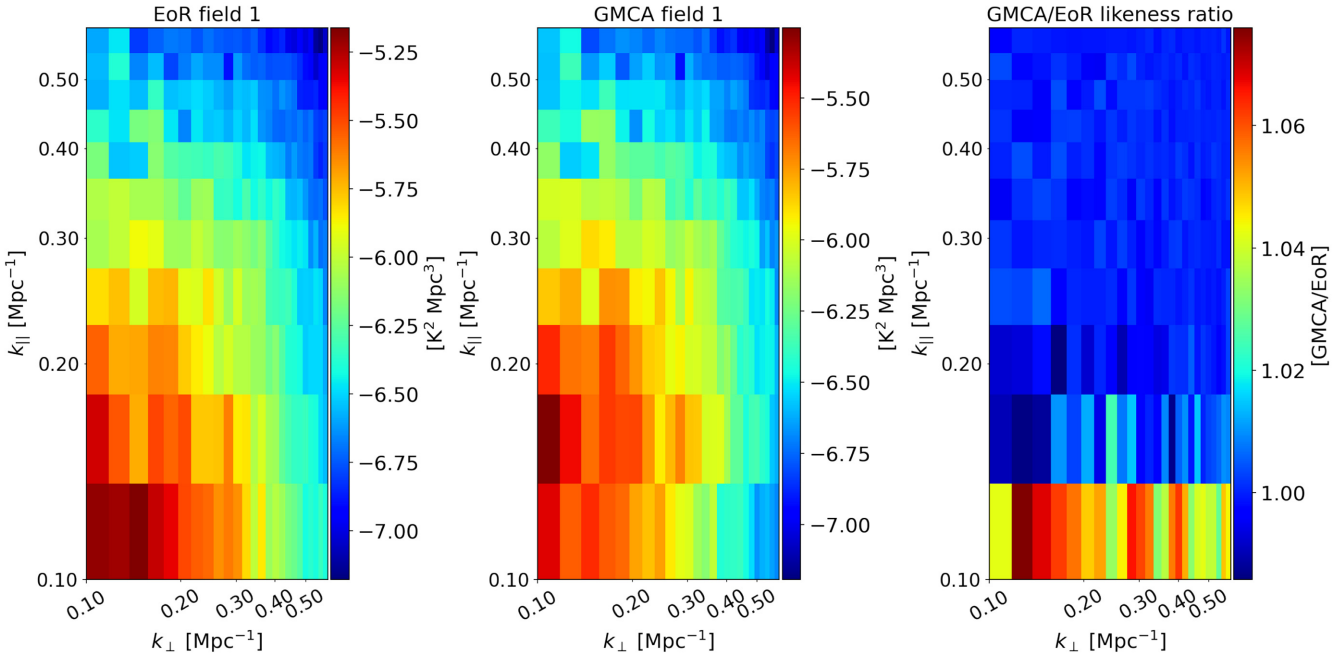

Figure B1. Here, from left to right, respectively, we compare the logarithm of the 2D power spectrum as measured from the clean EoR-only signal, the GMCA residuals (assuming four components and recovering FGs from 'observed' field 1) and the likeness ratio of the two. GMCA is very effective at recovering the 2D power spectrum of the clean EoR signal from the observed signal.

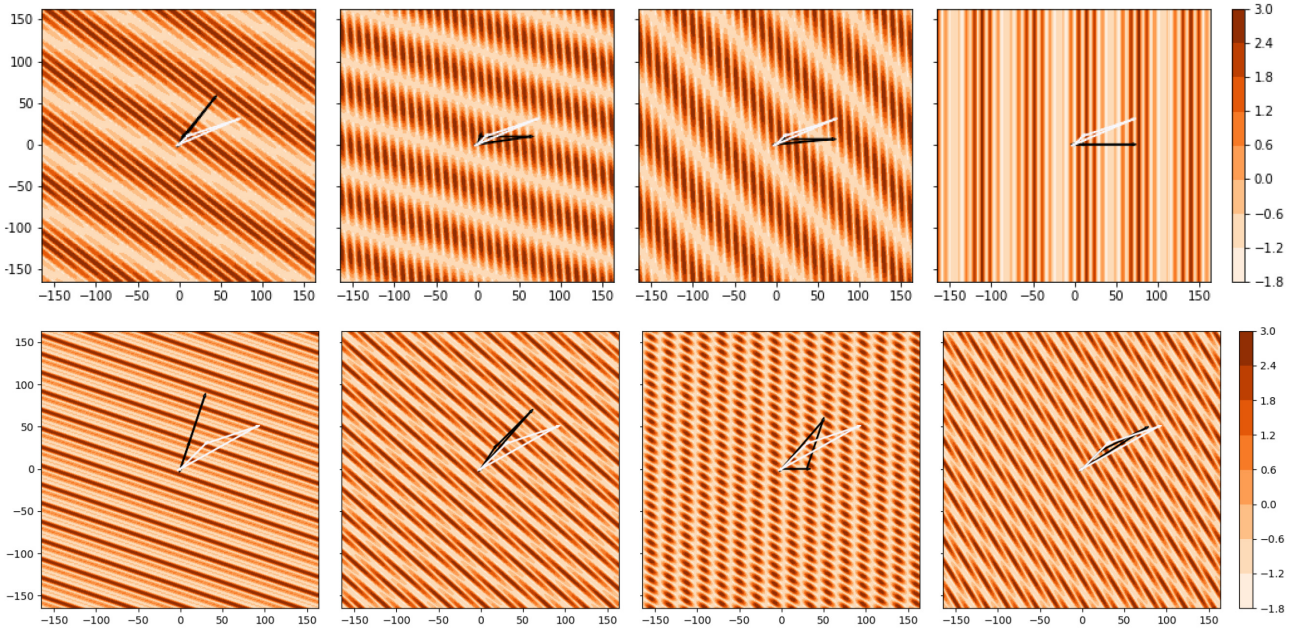

Figure C1. Interference patterns (projected on the perpendicular sky plane) for the waves associated with the Fourier transform for three k vectors that form a triangle. We show two configurations that exhibit an extreme FG bispectrum, one on each row. Each column corresponds to different k_x and k_y combinations that form $\boldsymbol{k}_1^{\rm perp}$ and $\boldsymbol{k}_2^{\rm perp}$. The white triangle shows the shape of the configuration and the black triangle shows its projection on to the perpendicular sky plane (both scaled up by 100). The top row corresponds to the $(k_1^{\rm perp}, k_1^{\rm los}) = (0.1\ {\rm cMpc}^{-1}, 0.1\ {\rm cMpc}^{-1})$ and $(k_2^{\rm perp}, k_2^{\rm los}) = (0.6\ {\rm cMpc}^{-1}, 0.1\ {\rm cMpc}^{-1})$ configuration and the bottom row to $(k_1^{\rm perp}, k_1^{\rm los}) = (0.3\ {\rm cMpc}^{-1}, 0.3\ {\rm cMpc}^{-1})$ and $(k_2^{\rm perp}, k_2^{\rm los}) = (0.6\ {\rm cMpc}^{-1}, 0.2\ {\rm cMpc}^{-1})$.

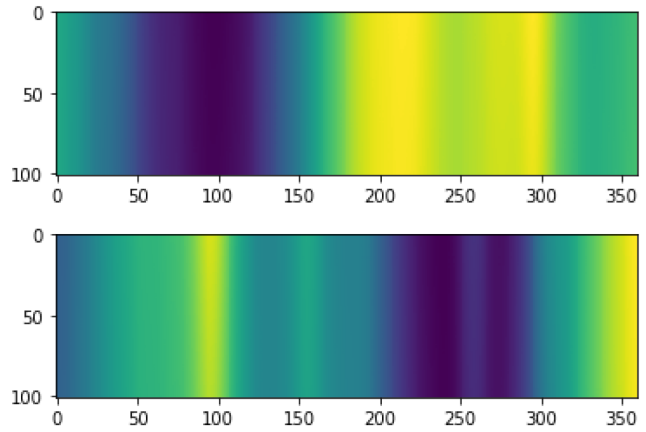

Figure C2. Maps from observed field 1 sliced along the frequency axis. We see strong bands of emission that drive a strong bispectrum for squashed configurations like those shown in Fig. C1. Axis labels are describe cMpc, with the shorter axis being the line of sight.

APPENDIX C: INTERPRETING THE FOREGROUND BISPECTRUM

While this paper is less concerned with gaining an in-depth understanding of what structures are driving the bispectrum than we have been in previous works, such as Watkinson et al. (2019), it is still interesting to consider what the interference patterns look like for configurations that exhibit a strong FG bispectrum. The Fourier transform for a particular $\boldsymbol{k}$ is associated with a plane wave through $e^{i\boldsymbol{k}x}$; as such, we can generate an interference pattern of the real parts of the three FFT waves of a given triangle configuration of k-vectors. This interference pattern informs us as to what structures a particular $\boldsymbol{k}$ triangle probes. The closer the structure in a data set to a $\boldsymbol{k}$-triangle's interference pattern, the stronger the bispectrum will be for that configuration. It is important to note that a given structure in a data set will produce a non-zero bispectrum for many different combinations of $\boldsymbol{k}_1, \boldsymbol{k}_2, \boldsymbol{k}_3$; i.e. there is not a one-to-one relation between the bispectrum for a particular $\boldsymbol{k}$-configuration and the real-space structures of your data.

Previous works have presented and discussed the real part of the interference patterns for particular $\boldsymbol{k}$-triangle shapes, which is useful for interpreting the spherically averaged bispectrum from a homogeneous and isotropic data set (Lewis 2011; Watkinson et al. 2019; Hutter et al. 2020). However, given that we are working with our $\boldsymbol{k}$ vectors parametrized into their perpendicular and line-of-sight components, the interpretation of this is more complex. In particular, for the FGs, the structure on the sky does not change as we scan through in the line of sight (although the intensity of the FGs does increase with decreasing frequency). We have therefore created an animation that scans through the various combinations for the x and y components of $k_1^{\rm perp}$ and $k_2^{\rm perp}$, for any given $(k_1^{\rm perp}, k_1^{\rm los})$ and $(k_2^{\rm perp}, k_2^{\rm los})$, and projects the associated interference pattern on to the perpendicular x–y plane.

In Fig. C1, we show a range of interference patterns from this animation for two different configurations. We include a range of k_x and k_y combinations to illustrate the different types of sky-structure probed by this configuration. The white triangles show the true shape of this triangle configuration, and the black triangle its projection on to the perpendicular x–y plane; both are scaled up by a factor of 100 from their natural scales.[16] Darker red shading denotes concentrations of above-average signal, or positive amplitude. In the top row of Fig. C1, we show a range of interference patterns for

[16]The amplitude (A) of each of the 3D plane waves that we sum to produce the interference patterns in Fig. C1, is described by $A = \cos(k_x x + k_y y + k_y z)$.

the $(k_1^{\rm perp}, k_1^{\rm los}) = (0.1\ {\rm cMpc}^{-1}, 0.1\ {\rm cMpc}^{-1})$ and $(k_2^{\rm perp}, k_2^{\rm los}) = (0.6\ {\rm cMpc}^{-1}, 0.1\ {\rm cMpc}^{-1})$ configuration (for which the FG-only bispectrum is strong and positive, as seen in the middle plot of Fig. 4). In the bottom row of Fig. C1, we show a range of interference patterns for the $(k_1^{\rm perp}, k_1^{\rm los}) = (0.3\ {\rm cMpc}^{-1}, 0.3\ {\rm cMpc}^{-1})$ and $(k_2^{\rm perp}, k_2^{\rm los}) = (0.6\ {\rm cMpc}^{-1}, 0.2\ {\rm cMpc}^{-1})$ configuration, for which the FG-only bispectrum is weekly negative (see the middle plot of Fig. 5) and therefore is driven by voids of FG emission. We see that there is a modulation of a large-scale mode over a small-scale mode; this produces bands of tightly packed ellipses of above-average signal.

Since we have seen from our analysis of the cross-bispectrum that filtering along the frequency-axis-only suppresses much of the non-Gaussianity in the FG data, it is likely that the bispectrum of FGs is dominated by structure in the frequency plane. We plot slices (taken along the frequency axis) of the observed field 1 in Fig. C2 (we opt to plot observed slices over clean ones as the observation smooths and thus decreases the dynamic range of the maps). There is clear banding in these maps, driven by point sources that have not been removed from the data set and regions of concentrated diffuse emission, it is this banding that drives the strong bispectrum we observe for these stretched and squeezed configurations.

This paper has been typeset from a TEX/LATEX file prepared by the author.